






## Article

# Ziziphus joazeiro Stem Bark Extract as a Green Corrosion Inhibitor for Mild Steel in Acid Medium

Aparecida Cristina Mauro <sup>1,\*</sup>, Bernardo Dias Ribeiro <sup>2</sup>, Rafael Garrett <sup>3</sup>, Ricardo Moreira Borges <sup>4</sup>, Talis Uelisson da Silva <sup>1</sup>, Sérgio de Paula Machado <sup>1</sup>, Joyce Rodrigues de Araujo <sup>5</sup>, Sanair de Oliveira Massafra <sup>5</sup>, Francisco Odencio Rodrigues de Oliveira Junior <sup>6</sup> and Eliane D'Elia <sup>1</sup>

<sup>1</sup> Department of Inorganic Chemistry, Chemistry Institute, Federal University of Rio de Janeiro, 149 Athos da Silveira Ramos Ave, Rio de Janeiro 21941-909, Brazil; talisus@iq.ufrj.br (T.U.d.S.); sergiopm@iq.ufrj.br (S.d.P.M.); eliane@iq.ufrj.br (E.D.)

<sup>2</sup> Department of Biochemical Engineering, Chemistry School, Federal University of Rio de Janeiro, 149 Athos da Silveira Ramos Ave, Rio de Janeiro 21941-909, Brazil; bernardo@eq.ufrj.br

<sup>3</sup> Metabolomics Laboratory, Chemistry Institute, Federal University of Rio de Janeiro, 1281 Horácio Macedo, Rio de Janeiro 21941-598, Brazil; rafael\_garrett@iq.ufrj.br

<sup>4</sup> Walter Mors Institute of Research on Natural Products, Federal University of Rio de Janeiro, Rio de Janeiro 21941-909, Brazil; ricardo\_mborges@yahoo.com.br

<sup>5</sup> National Institute of Metrology, Quality and Technology, 50 Nossa Senhora das Graças Ave, Duque de Caxias 25250-020, Brazil; jraraujo@inmetro.gov.br (J.R.d.A.); sanair.massafra@gmail.com (S.d.O.M.)

<sup>6</sup> Laboratory Cellular Ultrastructure, Institute Oswaldo Cruz, 4365 Brazil Ave, Rio de Janeiro 21040-900, Brazil; foroj78@gmail.com

\* Correspondence: acmauro@gmail.com



**Citation:** Mauro, A.C.; Ribeiro, B.D.; Garrett, R.; Borges, R.M.; da Silva, T.U.; de Paula Machado, S.; de Araujo, J.R.; de Oliveira Massafra, S.; de Oliveira Junior, F.O.R.; D'Elia, E. *Ziziphus joazeiro* Stem Bark Extract as a Green Corrosion Inhibitor for Mild Steel in Acid Medium. *Processes* **2021**, *9*, 1323. <https://doi.org/10.3390/pr9081323>

Academic Editor: Lukáš Richtera

Received: 1 June 2021

Accepted: 20 July 2021

Published: 29 July 2021

**Publisher's Note:** MDPI stays neutral with regard to jurisdictional claims in published maps and institutional affiliations.



**Copyright:** © 2021 by the authors. Licensee MDPI, Basel, Switzerland. This article is an open access article distributed under the terms and conditions of the Creative Commons Attribution (CC BY) license (<https://creativecommons.org/licenses/by/4.0/>).

**Abstract:** The aqueous extract of Joazeiro stem bark (EJSB) and its high molecular weight fraction (HMWF) were examined as potential corrosion inhibitors of mild steel in 1 mol L<sup>-1</sup> hydrochloric acid media, using weight-loss measurements, potentiodynamic polarization curves and an electrochemical impedance spectroscopy (EIS). Varying the concentration of the inhibitors from 100 to 800 mg L<sup>-1</sup>, the results show an increase in anticorrosive efficiency from 85.4 to 89.8 and 89.8 to 93.0% for EJSB and its HMWF, respectively, using the data of the gravimetric essay, and from 84.5 to 94.5 and 89.9 to 94.7% for EJSB and its HMWF, respectively, from the impedance data. The composition of the crude extract was chemically characterized by liquid chromatography-high resolution mass spectrometry. Additionally, scanning electron microscopy (SEM) and X-ray photoelectron spectroscopy (XPS) were used, respectively, to morphologically and chemically characterize the surface. Considering that the saponin molecules, the main constituent from juá, are responsible for its inhibitory action, quantum chemical calculations showed that the C67, C69 and O144 atoms likely have an important role in the process of electron-donation of saponin to metal, due to the higher values of  $f_k^+$  and %HOMO observed on these atoms.

**Keywords:** *Ziziphus joazeiro* stem bark extract; corrosion inhibitor; mild steel; LC-MS; electrochemical measurements

## 1. Introduction

Corrosion is a spontaneous process, resulting in the destruction of generally metallic materials, by chemical or electrochemical reactions with substances present in the medium. Corrosion is a very widespread, routine occurrence in that it mainly affects iron and its alloys, changing their characteristics, and making them unsuitable for their use and purpose [1,2]. Amongst the several methods of corrosion control and prevention in the metals, the use of corrosion inhibitors is one of the most effective, particularly in acidic environments, where it is necessary to avoid the metallic dissolution and its consumption by the acid [3]. Most organic inhibitors possess at least one functional group with an atom of oxygen, nitrogen, sulfur, or in some cases selenium and phosphorus and/or aromatic

ring and  $\pi$  electrons, through which can be adsorbed on the metallic surface. Usually, the inhibitory action of these compounds improves in the following order:  $O < N < S < P$  [4].

Although many synthetic compounds have shown a good anticorrosion effect, most of them are highly toxic, compromising health and the environment. The recognition of such toxic effects and increasing environmental concerns have led to research studies on inhibitors obtained from several parts of plants, including stalks, seeds, fruits, stem barks, and bagasse, which tend to be economical and non-toxic [5]. Vegetables, biomass waste and plant extracts have been understood to be renewable, environment-friendly, easily accessible and low-cost sources. In recent works, the use of biomass waste such as coconut shells, walnut shells, and corn silk has also been investigated as potential precursors for the preparation of low-cost carbon-based anodes [6–8].

These are made up of several compounds with several kinds of active ingredients, such as secondary metabolites, that represent many of the biological activities and adaptive processes of the plants [9,10]. While green inhibitors with different chemical structures have been contemplated as corrosion inhibitors, *Ziziphus joazeiro* extracts have not yet been reported in the literature for this particular use.

*Ziziphus joazeiro* is a tree native to the Brazilian semiarid region, in the caatinga biome, where it is popularly called “juazeiro”. It has economic potential for the hinterlands of Northeastern Brazil, to be used for ornamentation purposes, as an energy source, as a popular medicine, for production of cosmetic products and human and animal food, particularly during droughts [11].

Regarding the chemical composition of the *Ziziphus joazeiro* aqueous stem bark, steroids and saponins were reported as the major constituents, together with flavonoids [10–12]. Saponins are a class of compounds that are structurally characterized by the presence of a steroid-like glycoside. These saponins are produced by the plant's secondary metabolism and have been reported as corrosion inhibitors. They have a good corrosion-inhibition effect for mild steel in an acidic medium (HCl or H<sub>2</sub>SO<sub>4</sub>) [13–16]. The literature revealed the inhibitory effect of saponins extracted from *Gongronema latifolium* (SEGL) on mild steel in acid media. The inhibition efficiency was shown to be dependent on the concentration of SEGL, temperature, and the period of immersion. The optimum value of the inhibition efficiency for SEGL (96.5%) was obtained at an extract concentration of 0.5 g L<sup>-1</sup> [13].

In the present work, we describe for the first time the corrosion-inhibitory properties of the aqueous extract of *Ziziphus joazeiro* stem bark, assessed by weight loss measurements, electrochemical impedance spectroscopy and potentiodynamic polarization curves; the morphological and chemical analysis of the mild steel surface was performed by scanning electronic microscopy and X-ray photoelectron spectroscopy. Besides, the extracts were characterized by Energy-Dispersive Spectroscopy (EDS) and Liquid Chromatography-High Resolution Mass Spectrometry (LC-HRMS) analyses. Finally, theoretical calculations were carried out to interpret the inhibitory action of these compounds.

## 2. Materials and Methods

### 2.1. Materials

The *Ziziphus joazeiro* Mart. (Rhamnaceae) stem barks were obtained in a local market, compressed in size through the use of Willye knife-mills (Tecnal<sup>®</sup> TE-648, Tecnal, Piracicaba, SP, Brazil), and sifted (with Mesh Tyler32) to make the granulometry homogenous. The milled and sifted stem barks of *Z. joazeiro* (50 g) were extracted with distilled water for 24 h, under constant agitation at room temperature. The extract was filtered, frozen and lyophilized (Liotop L101, Liobras, São Carlos, SP, Brazil) to complete dryness. The extract of Joazeiro Stem Barks (EJSB) solid residue was stored at -4 °C until it was used.

The high molecular weight fraction (HMWF) was isolated from the EJSB by diafiltration. Briefly, the EJSB was submitted to an ultrafiltration 3 kDa cut-off membrane (Millipore) and centrifuged at 3800 rpm for 40 min. The fraction retained by this membrane (HMWF) was then washed with double distilled water and centrifuged. This fraction was frozen and lyophilized to yield the sample HMWF.

For the preparation of 1 mol L<sup>-1</sup> HCl solution, HCl (37%) (Merck KGaA, Darmstadt, Germany) was diluted in distilled water. The specimens were prepared with mild steel, according to the chemical composition shown in Table 1:

**Table 1.** Chemical Composition of mild steel (%m/m).

	C	P	S	Mn	Si	Fe
1020	0.18	0.04	0.05	0.30	Trace	Balance

## 2.2. Chemical Characterization

The chemical characterization of EJSB was carried out by Liquid Chromatography-Mass Spectrometry (LC-MS) and Energy-Dispersive Spectroscopy (EDS).

### 2.2.1. LC-MS Analysis of the Aqueous Extracts of Joazeiro Stem Barks

The EJSB samples ( $n = 3$ ) were dissolved in acetonitrile:water (1:1  $v/v$ ) and diluted to 1.0 mg mL<sup>-1</sup> in acetonitrile:water (3:7  $v/v$ ) before analysis.

The LC-MS analysis was performed in a hybrid quadrupole-orbitrap high-resolution mass spectrometer (QExactive Plus, Thermo Scientific, Frenton, CA, USA). The source parameters were spray voltage 3.9 kV (ESI<sup>+</sup>) and 3.6 kV (ESI<sup>-</sup>), capillary temperature 300 °C, source temperature 380 °C, S-lens RF level 50, sheath and auxiliary gases 45 and 15 arbitrary units, respectively. Data were obtained in full-scan mode over the  $m/z$  range of 120–1000, using a resolution of 35,000 followed by data-dependent MSMS experiment at a resolution of 17,500 and stepped normalized collision energy of 15–45%.

Sample components were separated in a reversed-phase C<sub>18</sub> column (Thermo Hypersil Gold 150 mm × 2.1 mm; 3.0 μm particle size) using an UltiMate 3000 UHPLC system (Thermo Dionex, Thermo Scientific, Frenton, CA, USA). Mobile phase A was 0.1% formic acid and 5 mmol L<sup>-1</sup> ammonium formate in water and mobile phase B was 0.1% formic acid in acetonitrile. The chromatographic separation was performed in gradient elution mode at a flow rate of 0.35 mL min<sup>-1</sup> as follows: 0–1 min 5% B, 1–16 min 95% B, 16–18 min 95% B, 18–22 min 5% B. The injection volume was 8 μL and the column temperature was 40 °C.

The raw data files from the EJSB samples and the sample solvent blank injection were converted to them zXML format into pairs for negative and positive ionization modes. Those files were then imported into MZMine2 for data processing to generate an aligned feature list across their MS/MS and chromatographic separation for each polarity [17]. The parameters used for data processing in MZMine2 are given in the Supplementary Information (SI) material. From the MZMine2, the exported .mgf aligned feature list for each polarity were submitted to the GNPS web server for feature-based molecular network (FBMN) analysis; then, their results were submitted to the GNPS Merge Network Polarity workflow for merging the different polarities as described at <https://github.com/mwang87/MergePolarity> (accessed on 1 June 2021) [18].

The FBMN for both positive and negative ionization modes is accessible at the GNPS website with the following links: (positive) <https://gnps.ucsd.edu/ProteoSAFe/status.jsp?task=3d44b80ca93b4d51ae154ef981be2626> (accessed on 28 May 2021); (negative) <https://gnps.ucsd.edu/ProteoSAFe/status.jsp?task=1e0529e7944041e7b2c5d20f28c8c1cb> (accessed on 28 May 2021); <https://gnps.ucsd.edu/ProteoSAFe/status.jsp?task=7205af7e7cf3412bb0230070d876fef9> (accessed on 28 May 2021) (merge polarity). GNPS parameters are given as SI. The resulting network was plotted using the Cytoscape software [16]. Concomitantly, those same .mzXML files were submitted to LipidXplorer for screening of expected saponins as they are considered to be the main secondary metabolite from the Zyziphus species, using the same protocol described elsewhere [19–22].

The results yielded by this last application were manually combined with the molecular network yielded by the GNPS workflow for annotation. Besides, compound annotation was also performed by comparing the experimental MS/MS spectra from compounds in

the extract to those available in the NIST MSMS 2014 library and Mass Spectra of North America (MoNA) [23].

#### 2.2.2. Energy-Dispersive Spectroscopy (EDS)

The elemental analysis through energy-dispersive spectroscopy (EDS) was obtained through a scanning electron microscope (Hitachi TM3030 Plus), with an acceleration voltage of 15 kV. The micrographs were obtained with a magnification of  $2000\times g$ .

#### 2.2.3. Quantification of Saponin

The quantification of saponins was confirmed by the Vanillin-Sulphuric acid method [24]. The standard curve was performed with diosgenin of  $1\text{ mg mL}^{-1}$  and the absorbance was detected by the spectrophotometer at 535 nm. All the analyses were repeated three times and the mean value of absorbance was obtained.

#### 2.2.4. X-ray Photoelectron Spectroscopy (XPS)

The XPS analysis was carried out in order to determine the surface composition and chemical states of the elements present in the EJSB and its high molecular weight fraction (HMWF) samples. X-ray photoelectron spectroscopy (XPS) was performed in ultra-high vacuum equipment (ScientaOmicron), using a non-monochromatic Al K $\alpha$  ( $h\nu = 1486.6\text{ eV}$ ) X-ray source, operated at 15 kV and 20 mA. The C 1s and N 1s high-resolution spectra were acquired with analyzer pass energy of 20 eV and 0.05 eV energy steps. The peak fitting was performed using CasaXPS software.

### 2.3. Weight Loss Essays

The weight loss measurements were carried out in the absence and presence of both EJSB and its HMWF at 100, 200, 400 and 800  $\text{mg L}^{-1}$  in  $1\text{ mol L}^{-1}$  HCl solution for 2 h immersion time at room temperature.

The weight loss essays were performed according to norm ASTM G31-7, by using analytical balance of 0.1 mg precision. Inhibition efficiency (IE%) was obtained through Equation (1) [1]:

$$\text{IE (\%)} = \frac{C_{R,0} - C_R}{C_{R,0}} \times 100, \quad (1)$$

where  $C_{R,0}$  is the corrosion rate ( $\text{g cm}^{-1}\text{ h}^{-1}$ ) in the absence of the inhibitor and  $C_R$  is the corrosion rate in the presence of the inhibitor.

Previously, the mild steel was mechanically abraded with 100, 320 and 600 grade sandpapers, washed with distilled water and ethanol, and then hot-air dried. The area of the specimens was measured by using a digital pachymeter. After being withdrawn from the test solutions, the mild steel specimen was washed with distilled water and ethanol and then dried.

Tests were carried out at different temperatures of 25, 35, 45 and 55 °C in both uninhibited and inhibited systems containing 200  $\text{mg L}^{-1}$  of the EJSB and its HMWF with 2 h immersion time.

### 2.4. Electrochemical Techniques

The electrochemical tests were performed in a model Autolab PGSTAT 128N potentiostat/galvanostat with a Metrohm impedance module. A 3-electrodes system was used with mild steel as the working electrode (with  $0.913\text{ cm}^2$  area), a large platinum wire as counter-electrode, and a saturated calomel electrode as reference.

In order to carry out the electrochemical impedance measurements, the open-circuit potential (OCP) was monitored for 8000 s. The impedance was carried out by frequency

ranging from 100 kHz to 10 mHz, with 10 points per decade and amplitude of 10 mV (rms). The inhibition efficiency (IE%) was calculated according to Equation (2) [1].

$$IE (\%) = \frac{R_p - R_{p,0}}{R_p} \times 100, \quad (2)$$

where  $R_p$  e  $R_{p,0}$  are the polarization resistances ( $\Omega \text{ cm}^2$ ) obtained, respectively, in the presence and absence of the inhibitor.

The anodic and cathodic potentiodynamic polarization curves were obtained using a scanning rate of  $1 \text{ mV s}^{-1}$  from  $-300 \text{ mV}$  to  $+300 \text{ mV}$  in relation to the stable open circuit potential. Corrosion current density ( $j_{corr}$ ), corrosion potential ( $E_{corr}$ ), Tafel anodic ( $\beta_a$ ) and cathodic ( $\beta_c$ ) constants were obtained by Tafel extrapolation method. Inhibition efficiency (IE%) was obtained by Equation (3) [1].

$$IE (\%) = \frac{j_{corr,0} - j_{corr}}{j_{corr,0}} \times 100, \quad (3)$$

where  $j_{corr,0}$  and  $j_{corr}$  are the corrosion current densities ( $\text{mA cm}^{-2}$ ), respectively, in the absence and presence of the inhibitor.

### 2.5. Scanning Electron Microscope (SEM) Studies

The surface morphological images of each investigated mild steel specimen, after immersion in  $1 \text{ mol L}^{-1}$  HCl, in the absence and the presence of  $200 \text{ mg L}^{-1}$  of the EJSB, and of the HWMF, with 2 h immersion time, employing a JEOL scanning microscope (JSM6390LV).

### 2.6. Theoretical Calculations

Density functional theory (DFT) calculations were conducted, using Gaussian 09 [25]. The optimized geometries of protonated (neutral) and non-protonated anion) of saponin were obtained using the functional B3LYP exchange-correlation hybrid [26,27] and the LanL2DZ pseudo-potential [28] was employed on all atoms. Calculations were conducted in the gas phase and the absence of imaginary frequency values in the optimized structures confirmed a minimal local energy.

The UCA-Fukui software [29] was used to obtain the reactivity Fukui indices using the Finite Difference approximation method (Equations (4) and (5)):  $q_k(N)$  is the charge on original structures and  $q_k(N - 1)$  and  $q_k(N + 1)$  are the charges on structures with one electron less and one electron more, respectively [30]. These indices also were obtained with the B3LYP/LanL2DZ theory level.

$$f_k^+ = q_k(N + 1) - q_k(N), \quad (4)$$

$$f_k^- = q_k(N) - q_k(N - 1), \quad (5)$$

The energies of frontier molecular orbitals (FMO,  $E_{HOMO}$  and  $E_{LUMO}$ ) were employed to obtain the following theoretical reactivity indices: hardness index ( $\eta$ , Equation (6)), Mulliken electronegativity ( $\chi$ , Equation (7)), electrophilicity ( $\omega$ , Equation (8)) and nucleophilicity ( $\varepsilon$ , Equation (9)) indices [30].

$$\eta = \frac{(E_{Lumo} - E_{Homo})}{2}, \quad (6)$$

$$\chi = -\frac{(E_{Lumo} + E_{Homo})}{2} \quad (7)$$

$$\omega = \frac{\chi^2}{4\eta} \quad (8)$$

$$\varepsilon = -\frac{1}{\omega} \quad (9)$$

The proton affinity (PA) was obtained by Equation (10):  $E_{prot}$  and  $E_{non-prot}$  are the total energies of protonated and non-protonated forms of the inhibitor, respectively, while  $E_{H_2O}$  and  $E_{H_3O^+}$  are the total energies of the  $H_2O$  and  $H_3O^+$ , respectively.

$$PA = E_{prot} + E_{H_2O} - E_{non-prot} + E_{H_3O^+} \quad (10)$$

### 3. Results

#### 3.1. Chemical Characterization

##### 3.1.1. LC-MS Analysis

The base peak chromatogram of the EJSB sample after background subtraction of the blank sample is shown in Figure 1 for both ESI ( $\pm$ ) analyses.

A total of 6 compounds were annotated in the samples by comparing their MS/MS spectra and exact mass measurement (error < 6 ppm), using the public (MoNA) and commercial (NIST MSMS 2014) databases in MS-DIAL software: agmatine ( $t_R$  0.7 min,  $[M+H]^+$ , error 2.4 ppm), aspartic acid ( $t_R$  0.8 min,  $[M+H]^+$ , error 4.7 ppm), gluconic or galactonic acid ( $t_R$  0.8 min,  $[M-H]^-$ , error 5.1 ppm), citric or isocitric acid ( $t_R$  0.8 min,  $[M-H]^-$ , error 4.0 ppm), *N*-acetylglutamic acid ( $t_R$  0.9 min,  $[M+H]^+$ , error 4.6 ppm), 3-Hydroxy-11-ursen-28,13-olide ( $t_R$  10.5 min,  $[M+H-H_2O]^+$ , error 1.9 ppm). Most of them are highly polar compounds eluted at the beginning of the chromatographic analysis in the reversed-phase column, resulting in the large peak observed around 0.8 min in Figure 1.

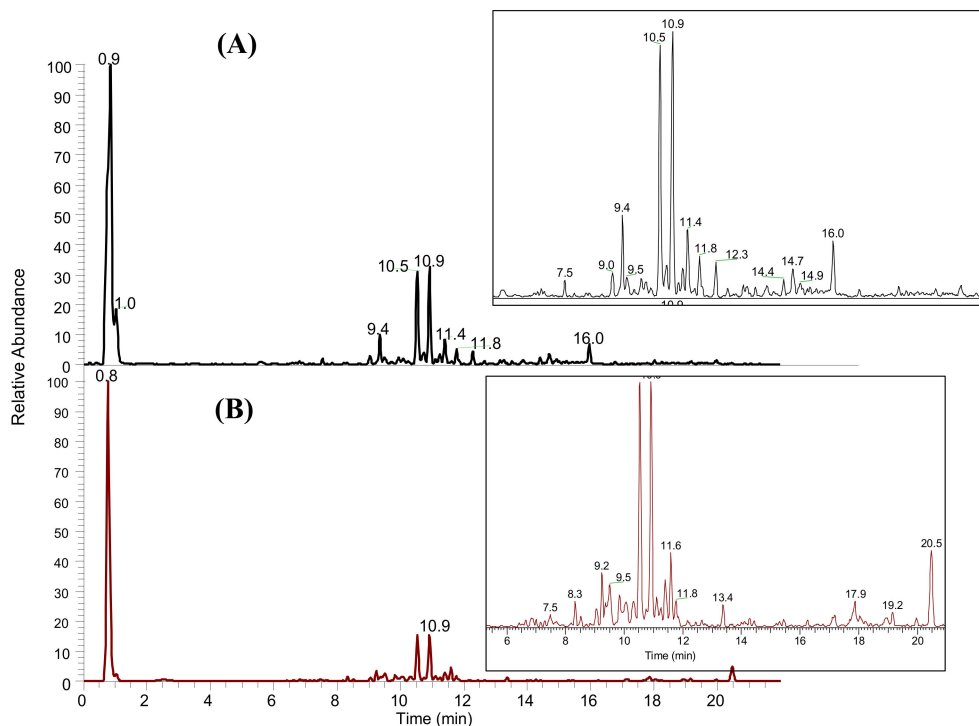


**Figure 1.** Base peak chromatogram of EJSB sample in (A) positive-ESI and (B) negative-ESI. The insert shows zoomed regions of the LC-HRMS chromatograms.

The LC-HRMS datasets from ESI-(+) and ESI(-) analyses were submitted to the FBMN for visualization of the chemical space of EJSB. Among the compounds detected, triterpenes and saponins were annotated as major constituents. GNPS did not yield any match with its database. The Lipid XPlorer approach enabled the annotation of 12 derivatives of cucurbitacins and jujubogines aglycones and glycosides (Supplementary Figure S1). It is virtually impossible to determine the unequivocal structure of each compound without

laborious purification procedures, but it is safe to say there is a broad range of compounds with similar structure composition at different hydroxylation stages due to the number of nodes and the common H<sub>2</sub>O neutral loss of 18.01 Da. The fragmentation pattern widely shared by the compounds within this network is in agreement with such structures closely related to the jujubogenin and pseudojujubogenin with fragments at  $m/z$  121.10, 201.1 and 315.23 [31]. Thus, sharing the same network, many compounds were annotated as mono-, bi- and tri-glycoside derivatives due to neutral loss of the characteristic molecular weight of pentose, and hexone of 132.04 and 162.05 Da, respectively (Supplementary Table S1) [32].

### 3.1.2. Element Analysis by Energy-Dispersive Spectroscopy (EDS)

As stated above, the secondary metabolites, such as flavonoids, steroids and saponins, are present in the *Ziziphus joazeiro* stem bark extracts. Energy-Dispersive Spectroscopy (EDS), which is a technique used for the elemental analysis or the chemical characterization of a sample, was used to broaden such knowledge on the aforementioned extract.

The mass percentage of the chemical elements found by EDS are shown in Table 2. The main composition of the EJSB and HMWF are C and O, which are characteristic of organic substances.

**Table 2.** Extracts—mass percentage of elements.

	Mass Percentage/(%)							
	C	O	N	K	S	P	Mg	Se
EJSB	47.3	41.4	6.11	3.08	1.26	0.51	0.40	0.05
HMWF	51.6	36.9	8.63	1.26	0.87	0.40	0.15	0.03

In general, phytochemical compounds are characterized by single functional groups that, in many cases, may contain hetero atoms. For example, saponins have a very large amount of oxygen in their macromolecule that appears at functional sites as hydroxyl groups and ether linkages, as shown in Figure 2 [13]. It is important to note that some molecules containing nitrogen have been detected by LC-HRMS in the EJSB sample as agmatine, aspartic acid and *N*-acetylglutamic acid (results shown in Section 3.1.1). The chemical structure shown in Figure 2 explains the presence of sulfur in the extracts.

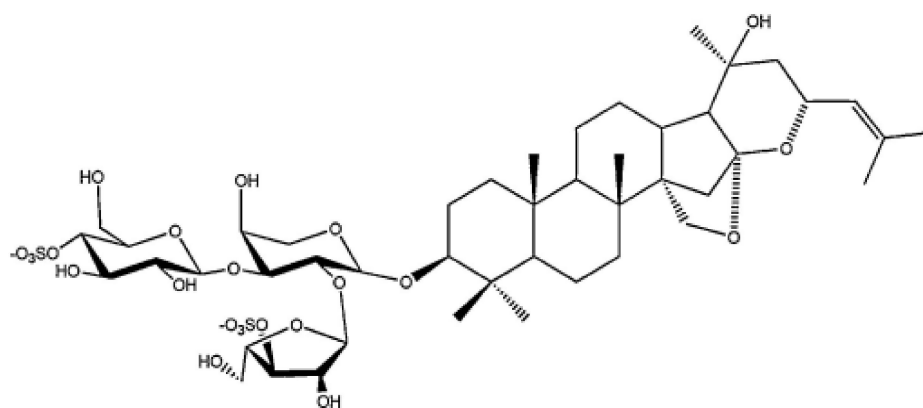


**Figure 2.** Saponin chemical structure from juá.

The presence of saponins and triterpenes was confirmed as main constituents by the LC-MS. Moreover, these compounds were reported by other studies as some of the main compounds which are present in the composition of the aqueous extract of the *Ziziphus joazeiro* stem bark [10–12,33].

### 3.1.3. X-ray Photoelectron Spectroscopy (XPS)

The XPS analysis was performed to investigate the surface composition and chemical states of the elements present in the samples, as well as the interaction of the organic film with mild steel support. Figure 3 presents the XPS survey spectrum for blank, EJSB and HMWF samples. Analyzing the survey's spectra, Figure 3a, it is possible to observe higher-carbon elemental content in the HMWF (~50%) in comparison with the EJSB (37%) and the blank samples (~20%). Oxidized-carbon elements content were similar between the studied samples (Table 3), but EJSB sample showed slightly more hydroxyl groups than HMWF sample, Figure 3b,c, respectively. Previous works (13) have been reporting that high-molecular weight saponins have a higher interaction with the support metal than the low-molecular weight saponins. In the present case, the binding energy of the iron element (Fe 2p photoelectron line) showed a peak shift when Fe 2p in EJSB and HMWF spectra are compared with Fe 2p in blank spectrum: from 710.6 eV in the blank spectrum to 709.6 eV for EJSB and 708.6 eV for HMWH sample. These binding energy values indicate an FeO (Fe II) oxidation state for all samples, but with different inhibitor-support at the interaction level [34]. The peak shifts observed in EJSB and HMWF indicate that oxygen atoms from the inhibitor films are donating electronic density to the metallic ion present in the mild steel support, decreasing its binding energy. Comparing the two investigated samples, HMWF presented higher inhibitor-support interaction.

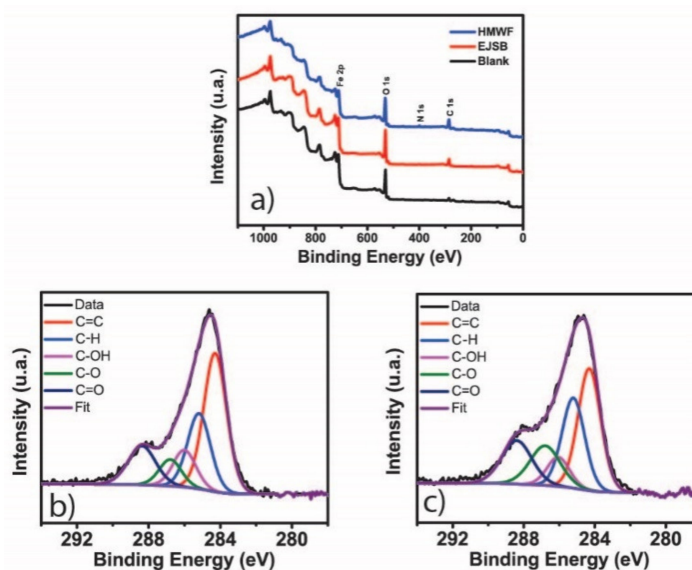


**Figure 3.** (a) X-ray photoelectron survey spectra showing the main chemical elements present in the three studied samples: EJSB, HMWF and blank; High resolution XPS spectra showing the chemical environment for C element (b) C1s for EJSB and (c) C1s for HMWF.

**Table 3.** Chemical composition in percentage evaluated from the Gaussian-Lorentzian (70/30) C 1s peak fitting.

	C=C (%) (284.6 ± 0.5 eV)	C-H (%) (285 ± 0.5 eV)	C-OH (%) (286.1 ± 0.5 eV)	C-O (%) (286.7 ± 0.5 eV)	C=O (%) (287.5 ± 0.5 eV)
EJSB	43	23	11	8	15
HMWF	35	26	8	15	16

The data above were evaluated from the C1s spectra deconvolution, and thus represent only an estimative of chemical composition to assist in the spectra interpretation. The peak position and full-width at half a maximum value were kept fixed, while the peak area was free to change in agreement with the best peak fit.

### 3.1.4. Saponins Content Quantification

The content of saponin in EJSB was determined from the regression equation of the calibration curve ( $y = 1.199x + 0.137$ ,  $R^2 = 0.972$ ), obtained using the colorimetric assay. In this present study, the saponin's content in fractions of the EJSB was  $0.488 \text{ mg mL}^{-1} \pm 0.129$  that corresponds to 65% ( $m/v$ ).



### 3.2. Weight Loss Essay

The weight loss essays were used to evaluate the inhibitory properties of aqueous EJSB and its HMWF for mild steel corrosion 1 mol L<sup>-1</sup> HCl solution (Table 4).

Table 4 shows the results of the weight loss measurements, using different concentrations of the aqueous EJSB and HMWF for 2 h immersion time. One can observe that as the concentration of both products EJSB and HMWF increases, the inhibition efficiency also increases. This suggests a protection mechanism due to the adsorption of molecules from the *Ziziphus Joazeiro* stem bark on the metal surface.

**Table 4.** Weight-loss measurements results for mild steel in 1 mol L<sup>-1</sup> HCl solution, in the absence and the presence of the aqueous EJSB and HMWF, at different concentrations.

[Inhibitor] (mol L <sup>-1</sup> )	EJSB			HMWF		
	C <sub>R</sub> (g cm <sup>-2</sup> h <sup>-1</sup> )	IE (%)	SD <sub>IE</sub> (%)	C <sub>R</sub> (g cm <sup>-2</sup> h <sup>-1</sup> )	IE (%)	SD <sub>IE</sub> (%)
Blank	1.49 × 10 <sup>-3</sup>	-	-	1.62 × 10 <sup>-3</sup>	-	-
100 ppm	2.24 × 10 <sup>-4</sup>	82.8	0.9	2.92 × 10 <sup>-4</sup>	82.7	0.7
200 ppm	2.25 × 10 <sup>-4</sup>	85.0	0.7	1.83 × 10 <sup>-4</sup>	90.1	0.6
400 ppm	1.88 × 10 <sup>-4</sup>	88.2	0.3	2.04 × 10 <sup>-4</sup>	89.0	0.6
800 ppm	1.67 × 10 <sup>-4</sup>	89.0	0.3	1.82 × 10 <sup>-4</sup>	90.5	0.6

C<sub>R</sub>—corrosion rate; IE—inhibition efficiency; SD—standard deviation.

Temperature is one of the factors that affects the corrosion of metals and the stability of inhibitive molecules on the metal surface [35]. Therefore, the influence of temperature on the inhibitory action of the aqueous EJSB and its HMWF was carried out for the mild steel corrosion in 1 mol L<sup>-1</sup> HCl solution.

As can be seen in Table 5, the corrosion rate increases with the temperature for both uninhibited and inhibited systems. However, such an increase is more significant in the absence of the extract. The IE (%) varied from 85% to 90% for EJSB and from 89% to 93% for HMWF, 25 to 55 °C. These results suggest that, as the temperature of the solution increases, the desorption of the water molecules of the metal surface is stimulated, resulting in an increase in the coverage of the surface by the inhibitive molecules.

The increase in IE, alongside the increase in temperature, may be due to the chemical interaction between the saponin molecules and the mild steel [36].

**Table 5.** Weight-loss data for mild steel in 1 mol L<sup>-1</sup> HCl solution, in the absence and presence of 200 mg L<sup>-1</sup> of the aqueous EJSB and of the HMWF from 25 to 55 °C.

T (°C)	Blank		EJSB		Blank		HMWF	
	C <sub>R</sub> (g cm <sup>-2</sup> h <sup>-1</sup> )	C <sub>R</sub> (g cm <sup>-2</sup> h <sup>-1</sup> )	IE (%)	SD <sub>IE</sub> (%)	C <sub>R</sub> (g cm <sup>-2</sup> h <sup>-1</sup> )	C <sub>R</sub> (g cm <sup>-2</sup> h <sup>-1</sup> )	IE (%)	SD <sub>IE</sub> (%)
25	1.94 × 10 <sup>-3</sup>	2.83 × 10 <sup>-4</sup>	85.4	0.5	1.78 × 10 <sup>-3</sup>	1.82 × 10 <sup>-4</sup>	89.8	0.6
35	3.53 × 10 <sup>-3</sup>	3.51 × 10 <sup>-4</sup>	90.1	0.5	3.38 × 10 <sup>-3</sup>	2.97 × 10 <sup>-4</sup>	91.8	0.4
45	6.07 × 10 <sup>-3</sup>	5.52 × 10 <sup>-4</sup>	90.9	0.2	6.31 × 10 <sup>-3</sup>	4.70 × 10 <sup>-4</sup>	92.6	0.0
55	1.04 × 10 <sup>-2</sup>	1.04 × 10 <sup>-3</sup>	89.8	0.2	1.08 × 10 <sup>-2</sup>	7.43 × 10 <sup>-4</sup>	93.0	0.3

C<sub>R</sub>—corrosion rate; IE—inhibition efficiency; SD—standard deviation.

The apparent activation energy of the system (*E<sub>a</sub>*) was obtained through Equation (11) [1].

$$\ln C_R = \frac{-E_a}{RT} + \ln A, \quad (11)$$

where C<sub>R</sub> is the corrosion rate (g cm<sup>-2</sup> h<sup>-1</sup>), *E<sub>a</sub>* is the apparent activation energy (kJ mol<sup>-1</sup>), *A* is the pre-exponential factor, *T* is the absolute temperature (K) and *R* is the constant of the ideal gases (8.314 J K<sup>-1</sup> mol<sup>-1</sup>).

The Arrhenius plots (Figure 4) were acquired using data presented in Table 6, where the angular coefficient was used to obtain the value of the apparent activation energy associated to the corrosion process of the mild steel in the HCl solution. It is important to note that both straight lines for uninhibited and inhibited systems are parallel, with a small decrease in the angular coefficient with the addition of the inhibitor.

As shown in Table 6, the energy activation values obtained in the presence of EJSB, as well as in the presence of its HWMF, were lower than those obtained in their absence. The decrease in the values of the apparent activation energy ( $E_a$ ) in the presence of inhibitors is characteristic of a chemisorption process [4,37].

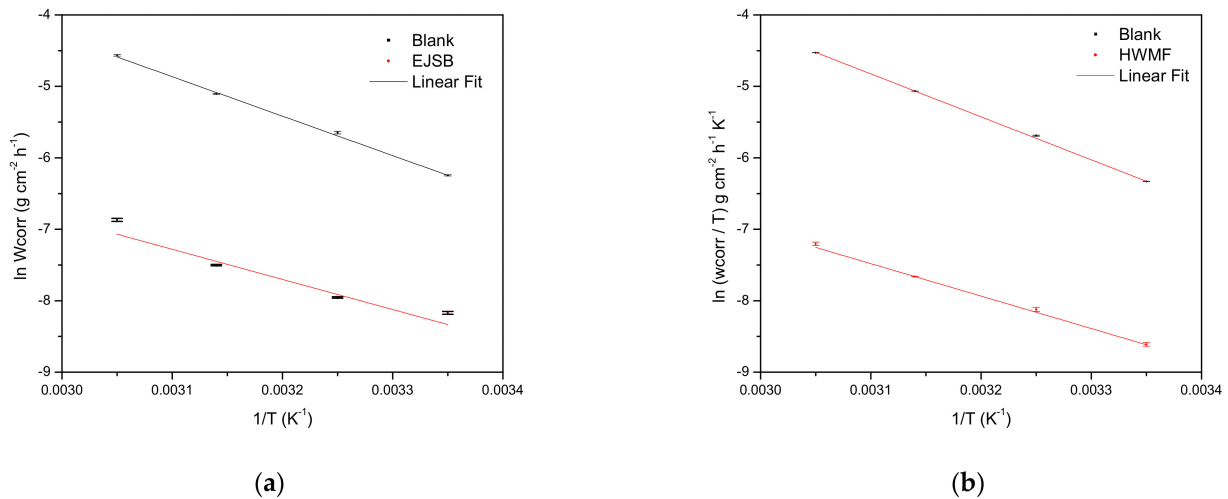


**Figure 4.** Arrhenius plots for mild steel in 1 mol L<sup>-1</sup> HCl solution in the absence and in the presence of: (a) EJSB and (b) HWMF.

**Table 6.** Activation parameters in the absence and presence of the aqueous EJSB and of the HWMF.

Inhibitor	$E_a$ (kJ mol <sup>-1</sup> )	$\Delta H^*$ (kJ mol <sup>-1</sup> )	$\Delta S^*$ (kJ mol <sup>-1</sup> K <sup>-1</sup> )
Blank	45.4	42.8	-153.3
EJSB	35.2	32.6	-204.4
Blank	49.1	46.5	-141.6
HWMF	38.1	35.5	-197.6

The activation parameters (activation enthalpy and entropy) were calculated by an alternative form of the Arrhenius Equation (12):

$$C_R = \frac{RT}{Nh} \exp\left(\frac{\Delta S^*}{R}\right) \exp\left(\frac{-\Delta H^*}{RT}\right), \quad (12)$$

where,  $h$  is the Planck constant ( $6.63 \times 10^{-34}$  J s),  $N$  is the Avogadro number ( $6.02 \times 10^{23}$ ) and  $\Delta S^*$  and  $\Delta H^*$  are the activation entropy and enthalpy, respectively.

The plot  $\ln(CR/T)$  vs.  $1/T$  (shown in Figure 5) produces a line with an angular coefficient of  $-\Delta H^*/R$  and a linear coefficient of  $\ln(R/Nh) + \Delta S^*/R$ , from which  $\Delta S^*$  and  $\Delta H^*$  are calculated and tabulated in Table 6.

The positive signs of the  $\Delta H^*$  reveals the endothermic nature of the mild steel dissolution process [38]. For both uninhibited and inhibited systems, the  $E_a$  values are greater than  $\Delta H^*$ , which suggests that the corrosion process involves a gaseous reaction. Activation entropies were negative in both the absence and the presence of the inhibitor, indicating that the activated complex in the determinant step is related more to a process of association than one of dissociation [1].

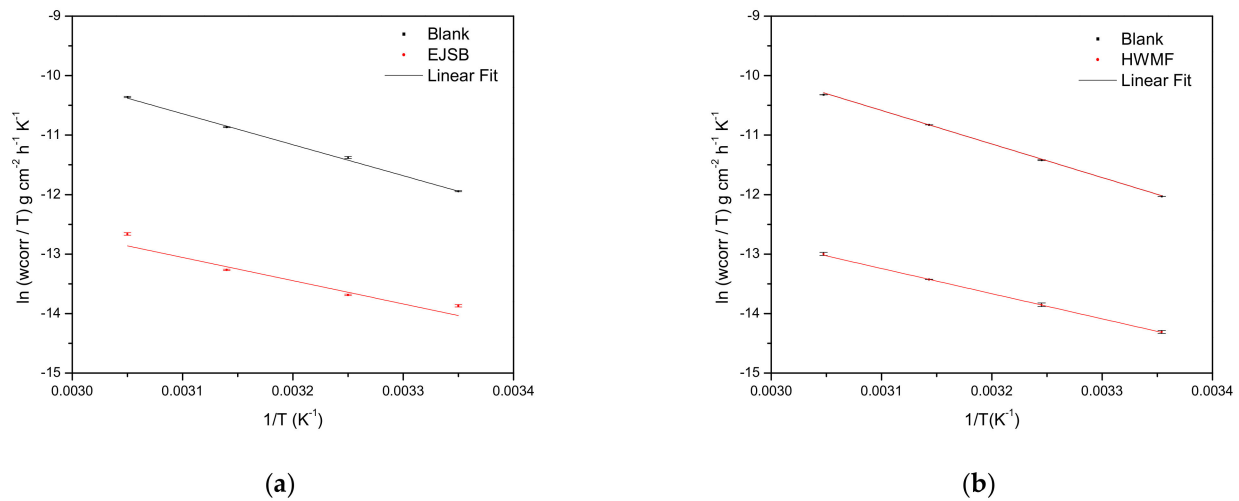


**Figure 5.** Arrhenius graph [ $\ln(w_{\text{corr}}/T)$  vs.  $1/T$ ] for mild steel in  $1 \text{ mol L}^{-1}$  HCl solution, in the absence and presence of: (a) EJSB and (b) HMWF.

### 3.3. Electrochemical Essays

#### 3.3.1. Open Circuit Potential

Before carrying out the electrochemical impedance and the potentiodynamic polarization curves, the OCP (open-circuit potential) was monitored until its stabilization.

The OCP was measured during 8000 s of exposure to the mild steel, both in the absence and the presence of the inhibitors. Figure 6 shows the OCP versus time graph. Initially, the OCP curves show a potential decrease for the first minutes of immersion, which could be related to the oxide-layer dissolution formed in the air.

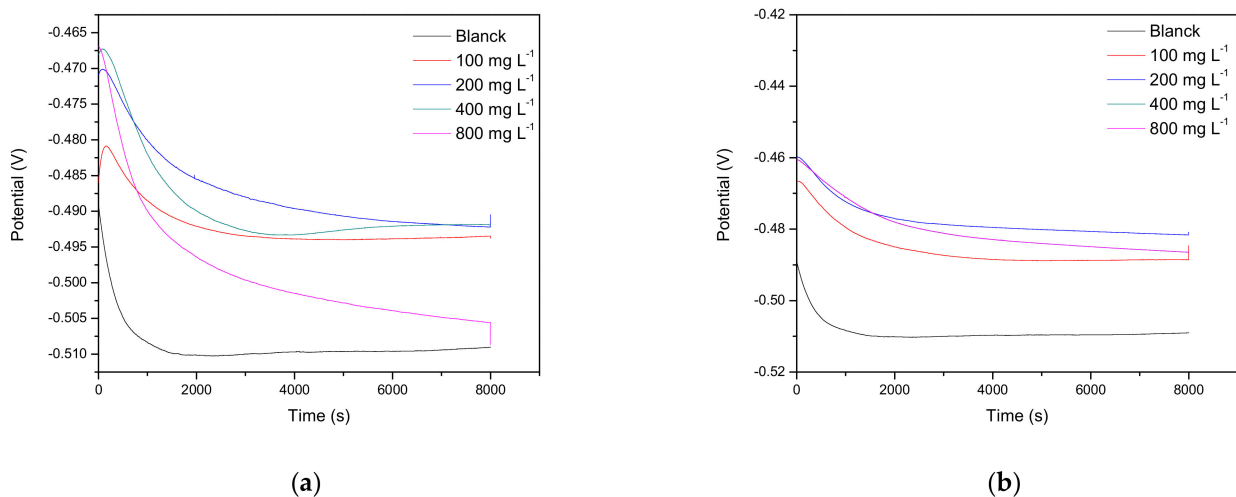


**Figure 6.** Variation of OCP as a function of time recorded for mild steel in  $1 \text{ mol L}^{-1}$  HCl solution, in the absence and the presence of different concentrations of total EJSB (a) and its HMWF (b).

From approximately 8000 s, the curves become horizontal, indicating that the OCP was stabilized in all cases.

The stabilized OCP values in the presence of the total EJSB and its HMWF were higher than the blank, with a maximum shift of 20 and 23 mV, respectively. These results indicate that the mild steel surface was modified by the molecules present in the extracts.

### 3.3.2. Electrochemical Impedance Spectroscopy (EIS)

Figure 7 shows Nyquist and Bode plots for mild steel in a 1 mol L<sup>-1</sup> HCl solution, in the absence and presence of several concentrations of the EJSB and its HWMF at room temperature.

The Nyquist diagrams show one capacitive loop flattened due to the lack of surface homogeneity and its roughness/rugosity [39]. The inhibitor addition did not change this behavior, indicating the activation-controlled nature of the reaction (Figure 7a,d). The increase in the inhibitor concentration leads to an increase in the diameter of the semicircle and thereby leads to higher polarization resistance ( $R_p$ ) values. This behavior is explained by the protection of the metal surface against the acid corrosion.

Figure 7b,e show a single time constant for all curves, without frequency shift in the presence of the inhibitor. Moreover, higher phase angles were obtained by the addition of inhibitors to the medium, indicating an increase in the surface capacitive behavior due to its inhibitory action against the corrosion. Also, in Figure 7c,f, we can see an increase in the impedance modulus with the inhibitor's concentration.

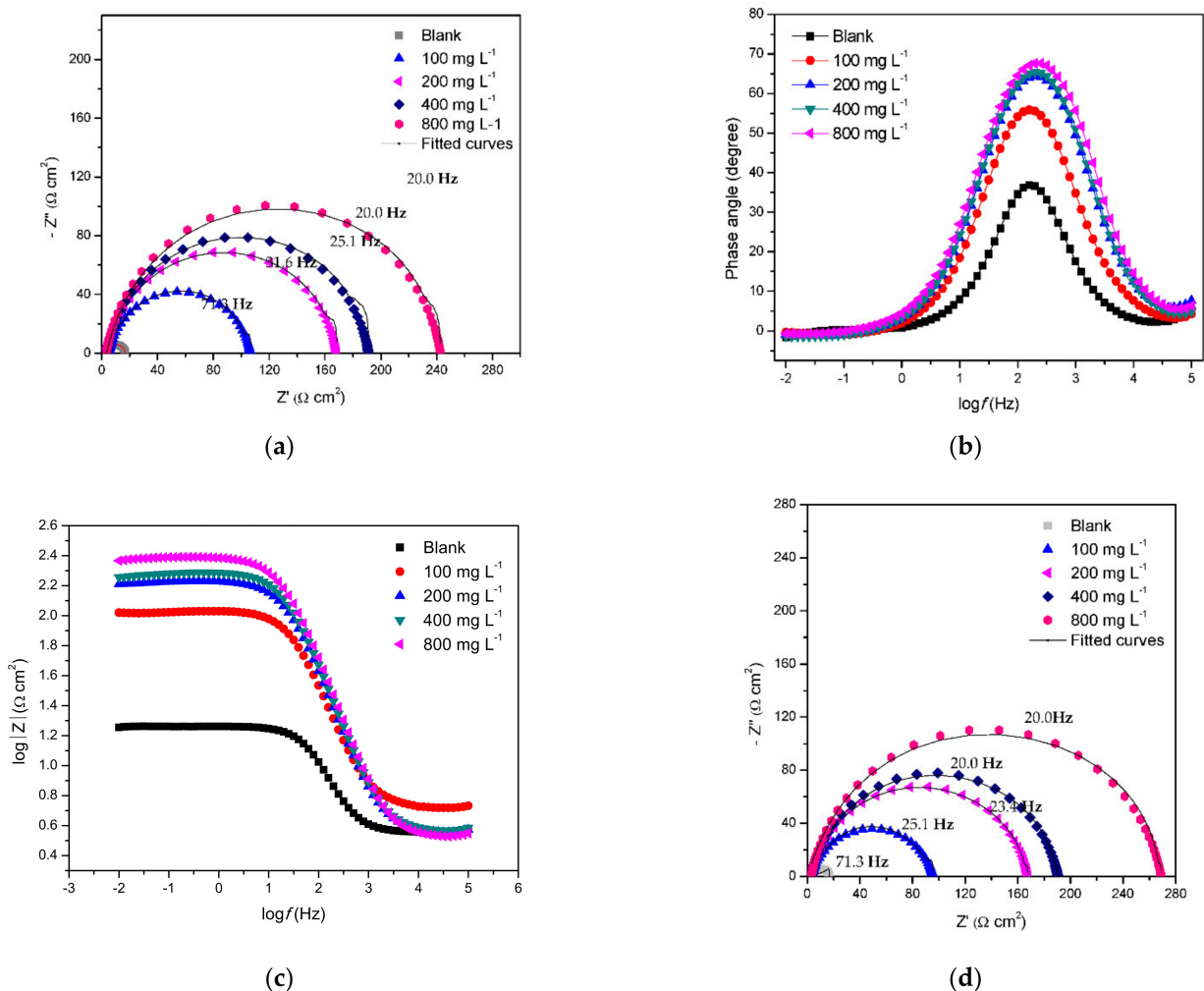
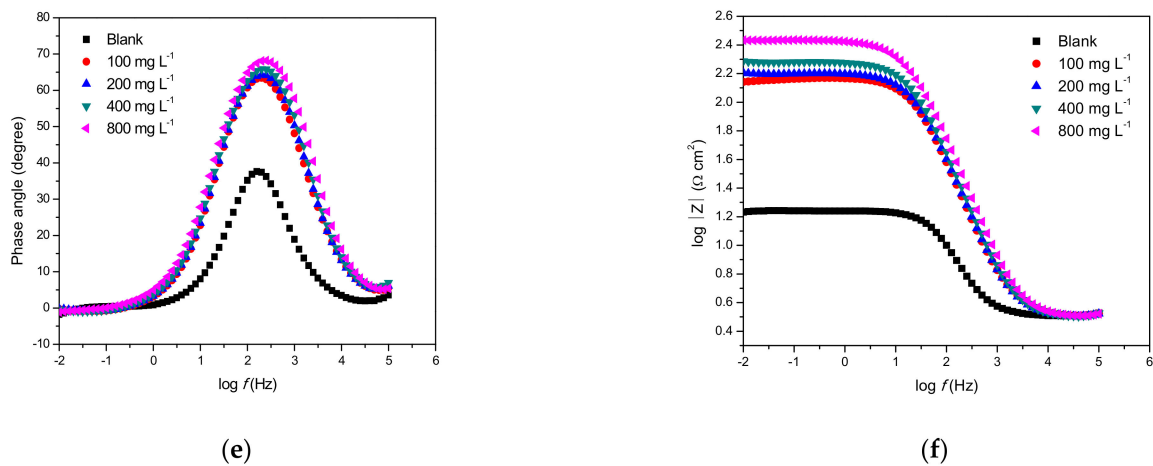


Figure 7. Cont.



**Figure 7.** Nyquist and Bode plots of mild steel in 1 mol L<sup>-1</sup> HCl solution, in the absence and in the presence of the EJSB and its HWMF: (a,d)—Z'' versus Z'; (b,e) phase angle versus frequency; and (c,f) impedance module versus frequency.

All impedance diagrams were analyzed based on an equivalent circuit, shown in Figure 8, where  $R_s$  is the solution resistance,  $R_p$  is the polarization resistance and CPE is the constant phase element, which was used instead of a double layer capacitor to provide a more precise adjustment.

The double layer capacitance ( $C_{dl}$ ), for a circuit including a CPE was calculated by Equation (13) [40]:

$$C_{dl} = Y_0 (2\pi f_{max})^{n-1}, \quad (13)$$

where,  $Y_0$  is the magnitude of CPE,  $n$  represents the deviation from the ideal behavior, and  $f_{max}$  is the frequency in which the imaginary component of the impedance is maximal.

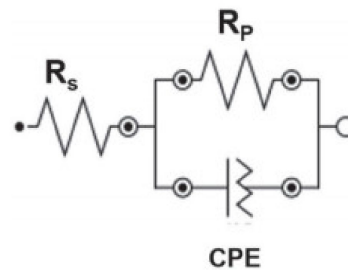


**Figure 8.** Equivalent circuit proposed for impedance data simulations.

Table 7 presents parameters as polarization resistance ( $R_p$ ), double-layer capacitance ( $C_{dl}$ ) and inhibition efficiency (IE%) for different inhibitor concentrations. The increase in the inhibitor concentration improves the  $R_p$  and reduces the  $C_{dl}$  values. The decrease in the  $C_{dl}$  values is due to the inhibitor molecules adsorption on the electrode surface, causing a reduction in the electroactive area [41].

The results obtained from weight loss measurements are in perfectly good agreement with those from electrochemical impedance studies. The IE varied from 85.4 to 89.8 and 89.8 to 93.0% for EJSB and its HMWF, respectively, using the gravimetric essays data and from 84.5 to 94.5 and 89.9 to 94.7% for EJSB and its HMWF, respectively, from the impedance data. Both EJSB and its HMWF show excellent inhibitory properties.

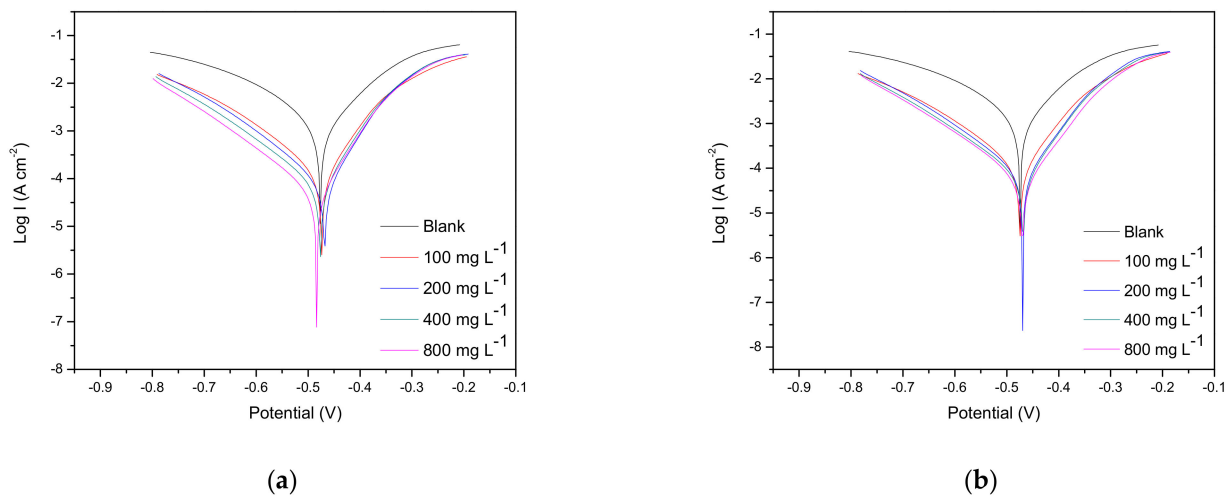
**Table 7.** Electrochemical parameters (EIS technique) in the absence and presence of the EJSB and of the HWMF, at different concentrations, in mol L<sup>-1</sup> HCl solution.

Inhibitor	[Extract]/(mg L <sup>-1</sup> )	<i>f</i> <sub>max</sub> /(Hz)	R <sub>p</sub> /(Ω cm <sup>2</sup> )	Y <sub>0</sub> /(μMho cm <sup>-2</sup> )	C <sub>dl</sub> /(μF cm <sup>-2</sup> )	<i>n</i>	IE/(%)	SD <sub>EI</sub> (%)
EJSB	0	71.3	15.5	273	146	0.904	-	-
	100	31.6	100	104	52.0	0.868	84.5	1.4
	200	25.1	149	78.9	43.0	0.881	89.1	3.2
	400	20.0	205	59.5	35.0	0.893	91.7	1.2
	800	20.0	271	55.2	33.0	0.889	94.5	0.2
HWMF	100	25.1	153	80.2	43.0	0.875	89.9	0.4
	200	23.4	171	76.8	42.0	0.878	90.9	0.3
	400	20.0	211	64.0	37.0	0.884	92.7	0.3
	800	20.0	291	54.0	31.0	0.884	94.7	0.0

*f*<sub>max</sub>—Frequency in which the imaginary component of the impedance is maximal; R<sub>p</sub>—Polarization resistance; Y<sub>0</sub>—Magnitude of CPE; C<sub>dl</sub>—Double layer capacitance; *n*—Deviation from the ideal behavior; IE—Inhibition efficiency; SD—Standard deviation.

### 3.3.3. Potentiodynamic Polarization Measurements

In Figure 9, the anodic and cathodic polarization curves were recorded for mild steel in 1 mol L<sup>-1</sup> HCl solution, with the absence and presence of different concentrations of the EJSB and its HWMF at room temperature. The electrochemical parameters, as corrosion potential (*E*<sub>corr</sub>), corrosion current density (*j*<sub>corr</sub>), anodic and cathodic Tafel slopes (*β*<sub>a</sub> and *β*<sub>c</sub>), were obtained from Tafel extrapolation method, and the corrosion-inhibition efficiencies IE (%) were calculated and presented in Table 8.

**Figure 9.** Potentiodynamic polarization curves for mild steel in 1 mol L<sup>-1</sup> HCl solution in the absence and presence of different concentrations of EJSB (a) and its HWMF (b).**Table 8.** Kinetic parameters obtained from the Tafel plots for mild steel in 1 mol L<sup>-1</sup> HCl solution in the absence and in the presence of EJSB and its HWMF at different concentrations.

Inhibitor	[Extract]/(mg L <sup>-1</sup> )	<i>E</i> <sub>corr</sub> /mV	<i>j</i> <sub>corr</sub> /(mA cm <sup>-2</sup> )	- <i>β</i> <sub>c</sub> /(mV dec <sup>-1</sup> )	<i>β</i> <sub>a</sub> /(mV dec <sup>-1</sup> )	IE/(%)	SD EI(%)
EJSB	0	-476	8.21 × 10 <sup>-1</sup>	101	86.7	-	-
	100	-471	1.31 × 10 <sup>-1</sup>	119	70.4d	84.0	0.4
	200	-470	8.34 × 10 <sup>-2</sup>	119	66.4	89.8	2.4
	400	-476	7.74 × 10 <sup>-2</sup>	124	67.5	91.3	0.9
	800	-487	5.10 × 10 <sup>-2</sup>	121	67.1	93.9	0.4
HWMF	100	-471	1.12 × 10 <sup>-1</sup>	123	75.6	86.4	0.0
	200	-465	8.37 × 10 <sup>-2</sup>	120	74.5	89.8	1.0
	400	-467	6.72 × 10 <sup>-2</sup>	127	68.4	91.8	0.3
	800	-470	5.87 × 10 <sup>-2</sup>	125	74.0	92.9	0.0

Polarization curve results showed that in the presence of EJSB and its HMWF there is a decrease in both anodic and cathodic current densities when compared to the system without an inhibitor. It is reported that if the shift in corrosion potential exceeds  $\pm 85$  mV, with respect to corrosion potential without an inhibitor, the inhibitor acts as anodic or cathodic type [37]. In the present case, the maximum displacement in  $E_{corr}$  is found to be  $-11$  mV and  $+6$  mV for EJSB and its HMWF, respectively, indicating that both EJSB and HMWF behave as a mixed type of inhibitor by acting on both hydrogen evolution and metal dissolution reactions through the adsorption on anodic and cathodic sites.

Table 8 shows that the addition of the EJSB and HMWF to the HCl solution results in a corrosion current density ( $j_{corr}$ ) decrease, while the inhibition efficiency increases as expected. This behavior could be attributed to the adsorption of the inhibitor molecules on the metal surface which, based on the weight loss tests varying temperature, appears to be chemical in nature [42]. Furthermore,  $\beta_a$  and  $\beta_c$  values varied very little with the addition of the extract. These results, combined with the impedance results, suggest that the molecules block the surface without changing the mechanism of cathodic and anodic reactions. However, the gravimetric essays showed an  $E_a$  decrease with the inhibitor addition for both EJSB and its HMWF. Therefore, the extract components probably act as a mixed type, where the screening effect is added to the activation effect [43].

### 3.4. Adsorption Isotherm

The adsorption isotherms help us to understand the mechanism of the interaction between the organic molecules and the metal surface [5,44]. The data obtained from the gravimetric essays were used to trace four types of adsorption isotherms: Langmuir, Temkin, Florry-Huggins and El-Awady. They relate the degree of surface coverage ( $\theta$ ) to the concentration of the inhibitor, according to Equations (14)–(17):

$$\frac{C}{\theta} = \frac{1}{K} + c, \quad (14)$$

$$\theta = \left( \frac{-2.303}{2a} \right) \log K + \left( \frac{-2.303}{2a} \right) \log c, \quad (15)$$

$$\log \left( \frac{\theta}{C} \right) = \log K + x \log(1 - \theta), \quad (16)$$

$$\log \left( \frac{\theta}{1 - \theta} \right) = \log K + y \log c, \quad (17)$$

$$\theta = \frac{IE}{100}, \quad (18)$$

where  $c$  is the concentration of the inhibitor ( $\text{mg L}^{-1}$ ),  $K$  is the constant equilibrium of adsorption,  $a$  is the lateral interaction parameter between the adsorbed molecules,  $x$  is the number of adsorbed water molecules replaced by the inhibitor molecules and  $y$  is the number of inhibitor molecules adsorbed in each active site.  $\theta$  ( $IE/100$ ) is the degree of surface coverage by the inhibitor molecule.

Table 9 shows all straight lines data obtained from the linear adjustments for both inhibitors (EJSB and its HMWF). The model that fitted the data best for both inhibitors (EJSB and its HMWF) is the Langmuir isotherm model. According to this model, it is assumed that the solid surface consists of a fixed number of adsorption sites and each site holds one adsorbed species [5].

Despite the good linear correlation ( $R^2 = 0.9999$ ) from the Langmuir isotherm, the angular coefficient deviated from one unit (1.040 and 1.046), for EJSB and its HMWF, respectively. These results suggest that there is interaction between adsorbed molecules of the inhibitor and/or the relation between active site for each adsorbed molecule is different from one unit [45].

**Table 9.** Data of straight lines obtained by linear adjustment for all isotherms.

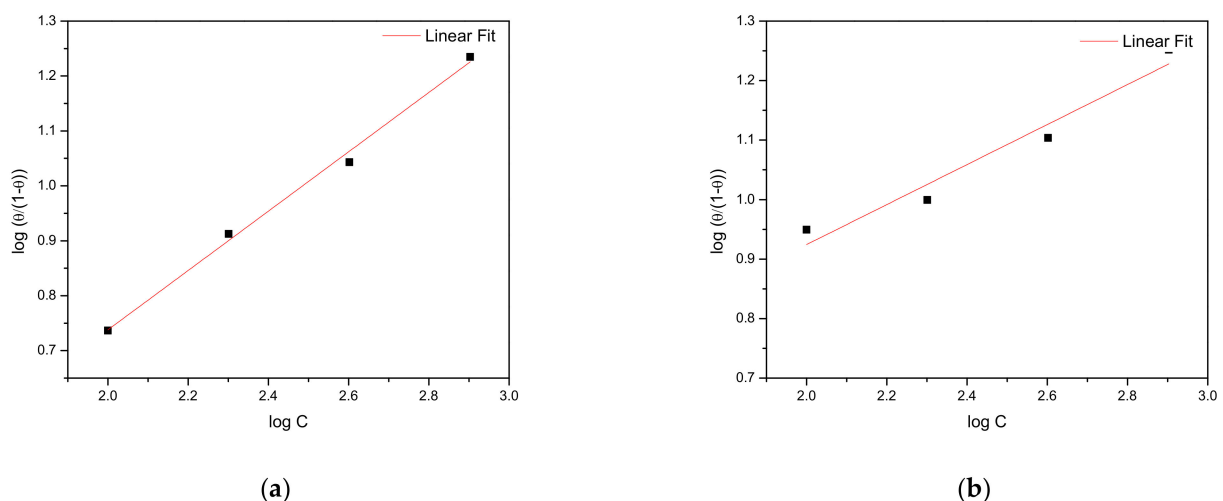
Isotherm	Linear Equation	R <sup>2</sup>
EJSB		
Langmuir	$y = 1.040x + 16.567$	0.9999
El-Awady	$y = 0.540x - 0.3427$	0.993
Flory-Huggins	$y = 1.932x - 0.512$	0.9915
Temkin	$y = 0.108x + 0.634$	0.9709
HMWF		
Langmuir	$y = 1.046x + 9.635$	0.9999
El-Awady	$y = 0.336x + 0.252$	0.9549
Flory-Huggins	$y = 2.983x + 0.830$	0.926
Temkin	$y = 0.054x + 0.789$	0.97

Flory-Huggins and El-Awady isotherms provide supplementary information. If the parameter  $x$  is greater than one unit, there is an indication that more than one molecule of water is displaced by a single molecule of the inhibitor. Similarly, if the parameter  $y$  is less than one unit, it shows that a single molecule of the inhibitor may be adsorbed on more than one active site of the metal [1,39,40,42]. Our results ( $x = 1.932$  and  $y = 0.540$  for EJSB and  $x = 2.983$  and  $y = 0.336$  for its HMWF) suggest that the inhibitory molecules are likely to be bulky. Besides, the parameter  $a$  from Temkin isotherm is negative, indicating the repulsive nature of the interaction between the adsorbed molecules. This supports the hypothesis that saponins are the molecules responsible for the inhibitory action of EJSB and its HMWF.

Considering that the inhibitory molecules are bulky, in addition to the Langmuir isotherm, the experimental data also fitted well into the thermodynamic-kinetics model of El-Awady (Figure 10) [46], where the binding constant  $K$  is given by [47]:

$$K = K'(1/y), \quad (19)$$

Large values of  $K$  mean a better and stronger interaction between the inhibitory molecule and the metal surface. For EJSB and its HMWF we found 0.2321 and 5.6138 as  $K$  values.

**Figure 10.** El-Awady adsorption isotherm of EJSB (a) and its HMWF (b) on mild steel in 1 mol L<sup>-1</sup> HCl at room temperature.

### 3.5. Scanning Electron Microscope (SEM) Studies

The Figure 11a,b presents the surface image of the abraded sample prior to and succeeding immersion in 1 mol L<sup>-1</sup> HCl solution for 2 h, whereas Figure 11c,d are the images of the mild steel surface after immersion in the corrosive solution, containing both



inhibitors EJSB and its HMWF, respectively. Figure 11b shows that the surface is highly damaged due to the formation of corrosion products and the attack of the aggressive solution in the absence of inhibitors. The image of the mild steel surface in the presence of the inhibitors, shown in Figure 11c,d, represents a surface which is smooth in comparison to Figure 11b. These results indicate that the presence of both inhibitors, EJSB and its HMWF, hinders the dissolution of the mild steel due to the formation of a protective film by the adsorption of inhibitor molecules onto the surface, which decreases the corrosion rate of mild steel in  $1 \text{ mol L}^{-1}$  HCl solution.

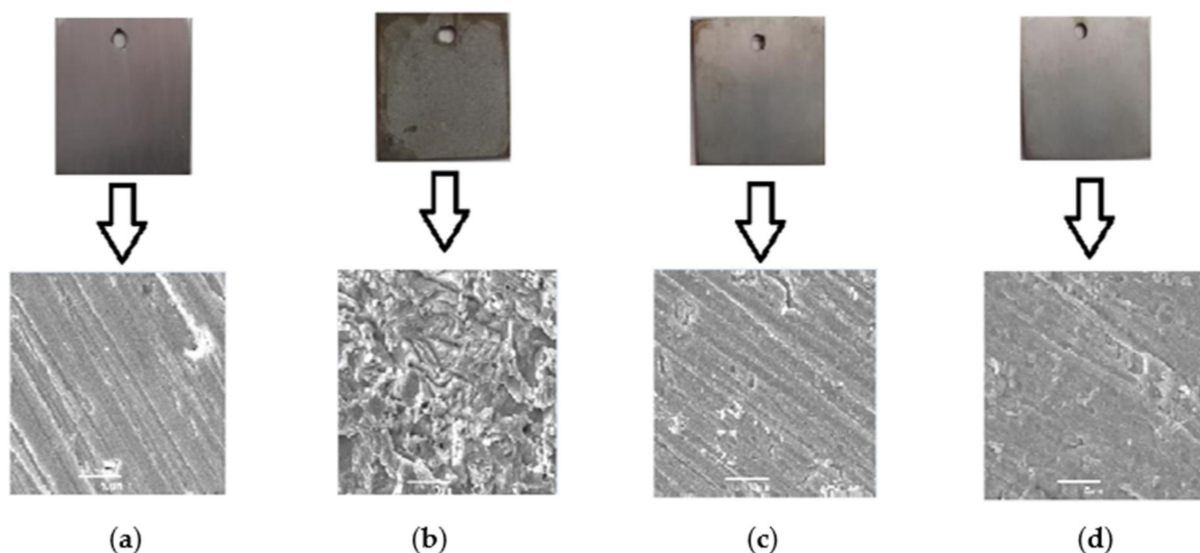


**Figure 11.** Photographs (on top) and SEM micrographs (on the bottom): abraded mild steel before immersion in the corrosive solution (a); immersion in  $1 \text{ mol L}^{-1}$  HCl without inhibitor (b); immersion in  $1 \text{ mol L}^{-1}$  HCl containing  $200 \text{ mg L}^{-1}$  of EJSB (c); immersion in  $1 \text{ mol L}^{-1}$  HCl containing  $200 \text{ mg L}^{-1}$  of HMWF (d).

### 3.6. Theoretical Calculations

The PA (Equation (10)) was calculated for saponin with O120 and O136-atoms from -SO<sub>4</sub> groups (Figure 12) protonated and deprotonated since in acid environment the molecule must be protonated. The value obtained ( $-13.69 \text{ kcal mol}^{-1}$ ) suggests that the protonation in these O atoms is favorable.

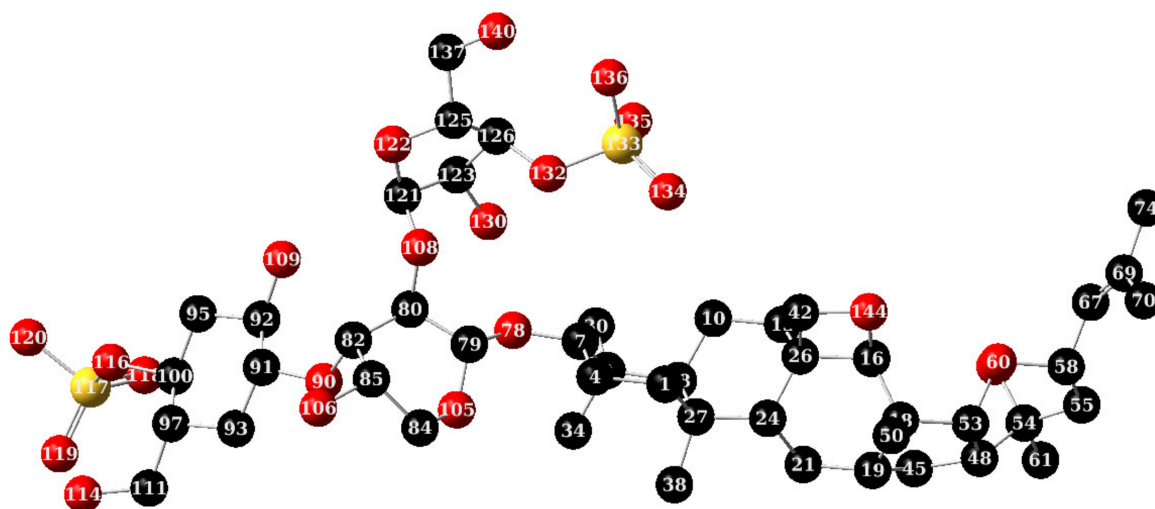


**Figure 12.** Numbered optimized structure calculated for saponin (protonated form) by B3LYP/LanL2DZ level with PCM model.

The FMO energies are associated with the ability of donation ( $E_{HOMO}$ ) and acceptance ( $E_{LUMO}$ ) of electrons and corrosion inhibitors in the redox process. A higher  $E_{HOMO}$  indicates a higher electron's donation from the inhibitor to the metal surface, while a lower  $E_{LUMO}$  indicates a higher electron's donation from the metal surface to the inhibitor [30]. A lower  $gap_{HOMO-LUMO}$  ( $E_{LUMO}-E_{HOMO}$ ) implies a high stability for the inhibitor-metal complex which has formed [48]. The  $E_{HOMO}$  and  $E_{LUMO}$  calculated (Table 10) showed that both forms of saponin have a similar  $E_{HOMO}$  values. The protonated form presented alower  $E_{LUMO}$  than the non-protonated form. Thus,  $E_{LUMO}$  suggests that the protonated form of the inhibitor should have better electron-accepting ability from the metal surface than the non-protonated form. In addition, the lower  $Gap_{HOMO-LUMO}$  of the protonated form indicates that this form has a higher reactivity than the non-protonated form.

The  $\eta$  index (Equation (6)) values showed that the protonated form has a lower-charge transferring resistance than the non-protonated form, while the  $\chi$  values (Equation (7)) showed that the protonated form has a higher electron attraction ability toward itself than the non-protonated form. The  $\omega$  (Equation (8)) index showed that the non-protonated form has a higher attraction to electron-rich centers than the protonated form, while  $\epsilon$  (Equation (9)) values showed that both forms have a similar attraction to electron-poor centers.

**Table 10.** Quantum Chemical global parameters (eV) for saponin by B3LYP/LanL2DZ level with PCM model.

Isotherm	$E_{HOMO}$	$E_{LUMO}$	$Gap_{HOMO-LUMO}$	$\eta$	$\chi$	$\omega$	$\epsilon$
Non-prot	-6.62	-2.16	4.47	2.23	-4.39	10.75	0.09
Prot	-6.67	-3.97	2.70	1.35	-5.32	9.56	0.10

In addition to the global parameters of reactivity, we calculated the local parameters of reactivity. As the protonated form showed the best results for the global parameters, the local parameters were only calculated for the protonated structure. The (Supplementary Table S2) presented the local parameters for the main atoms of inhibitor, while the (Supplementary Table S3) presented the local parameters for all the atoms of the structure.

The FMO graphical representations (Figure 13) showed that HOMO was localized in the regions of C67, C69 and O144 atoms, in which these atoms presented 9.565, 8.424 and 7.036% of contribution in HOMO, respectively (Supplementary Table S2). Additionally, it observed a strong  $\pi$  participation of the orbitals in these atoms.

The LUMO was localized in  $-SO_4$  group of S133-atom (Figure 13). This group presented 64.71% of the contribution in LUMO (Supplementary Table S2). These results suggest that the regions of the inhibitor that interact with metal surface are the C67=C69 bond and the O144-atom, which are both electron-rich regions (higher transfer of electrons from the inhibitor to the metal surface), and the region of  $-SO_4$  group, which is an electron-poor region (higher transfer of electrons from the metal surface to the inhibitor). Similar results were observed for non-protonated forms of saponin.

The analysis of the charge distribution of Mulliken (Supplementary Table S2) showed that the highest and lowest values of charge were observed in the S-atoms and the O-atoms, respectively. The atoms of the regions C10-C74 (and O144-atom) presented lower charge values, suggesting that this region of the molecule should interact with the metal surface by electron-donation, while the S-atom should accommodate the negative charge from the metal.

The changes in the chemical potential of a given atom of a molecule can be explained by the Fukui functions, which represent the change in electrons in one atom. The  $f_k^+$  and  $f_k^-$  functions correspond to the ability of one atom to receive and donate electrons, respectively [49]. Analyzing the results of (Supplementary Table S3), it observed that the atoms of this group have a high  $f_k^-$  and %LUMO values and the S133-atom has a higher charge value, suggesting that this group should better accommodate negative

charge from the metal surface. The higher values of  $f_k^+$  and %HOMO observed on the C67, C69 and O144 atoms suggest that these atoms have an important role in the processes of electron-donation of saponin to metal surface.

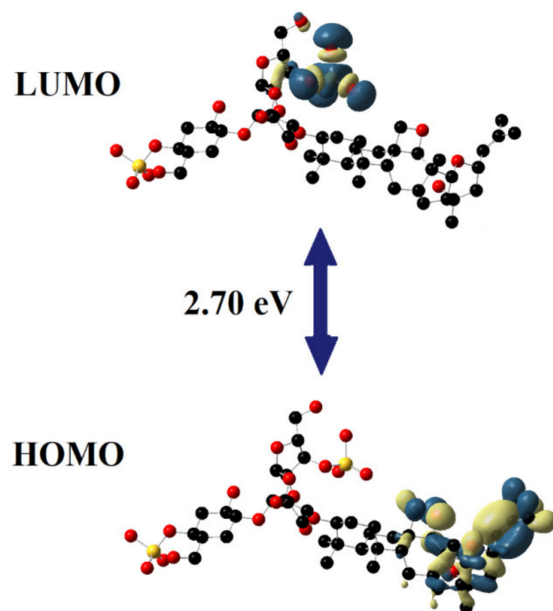


**Figure 13.** Graphical representations of HOMO and LUMO of structure calculated for saponin (protonated form) by B3LYP/LanL2DZ level with PCM model.

#### 4. Conclusions

The aqueous extract of Joazeiro Stem Barks (EJSB) and its high molecular weight fraction (HMWF) acts as a great corrosion inhibitor in an acid medium of 1 mol L<sup>-1</sup> HCl. The results achieved by gravimetric, weight loss method, electrochemical-impedance spectroscopy and anodic and cathodic polarization curves corroborate with each other. The anticorrosive efficiency augments with the concentration of both products EJSB and HMWF. The mechanism of inhibition occurs through adsorption on the metal surface, preventing both iron dissolution and hydrogen evolution, being, therefore, a mixed inhibitor, as shown by the potentiodynamic polarization curves. Electrochemical results showed that the addition of the extracts did not change the anodic and cathodic mechanism. However, the gravimetric essay's varying temperature showed the  $E_a$  decrease with the addition of the inhibitor for both EJSB and its HMWF. Therefore, the extract components probably act as a mixed type where the screening effect is added to the activation effect. The experimental data obtained in this study fits the thermodynamic-kinetic model of El-Awady. The chemical characterization of the EJSB by LC-MS analyses made the identification of 18 compounds possible. Among the compounds detected, saponins were annotated as major constituents which have structural characteristics necessary to adsorb on the metal surface and form a protective film. Considering the saponins as major constituent in EJSB, it is possible to suggest that they should be responsible for the adsorption process. From the theoretical study with the saponin found in juá, the higher values of  $f_k^+$  and %HOMO observed on the C67, C69 and O144 atoms suggest that these atoms have an important role in the processes of electron-donation of saponin to metal surface.

**Supplementary Materials:** The following are available online at <https://www.mdpi.com/article/10.3390/pr9081323/s1>, Figure S1: Network, Table S1: Compound annotation of main the saponins from EJSB from the positive-ESI, Table S2: Quantum Chemical local parameters for saponin by B3LYP/LanL2DZ level with PCM model, Table S3: Quantum Chemical local parameters for saponin by B3LYP/LanL2DZ level with PCM model.

**Author Contributions:** Conceptualization, A.C.M., B.D.R. and E.D.; Formal analysis, R.G., R.M.B., T.U.d.S., S.d.P.M.; Investigation, A.C.M., R.G., R.M.B., T.U.d.S., S.d.P.M., J.R.d.A., S.d.O.M. and F.O.R.d.O.J.; Methodology, A.C.M., B.D.R. and R.M.B.; Writing—original draft, A.C.M., R.G., R.M.B., T.U.d.S., S.d.P.M., J.R.d.A., E.D.; Writing—review & editing, A.C.M., R.G., R.M.B., T.U.d.S., S.d.P.M., J.R.d.A., E.D. All authors have read and agreed to the published version of the manuscript.

**Funding:** This research received no external funding.

**Data Availability Statement:** Not applicable.

**Acknowledgments:** The authors thank CNPq (Conselho Nacional de Desenvolvimento Científico e Tecnológico) for financial support (process number 424306/2016-6 and 312005/2018-0) and the Platform of Electron Microscopy of Institute Oswaldo Cruz for the use its facilities.

**Conflicts of Interest:** The funders had no role in the design of the study; in the collection, analyses, or interpretation of data; in the writing of the manuscript, or in the decision to publish the results.

## References

- Santana, C.A.; Cunha, J.N.; Rodrigues, J.G.A.; Greco-Duarte, J.; Freire, D.M.G.; D'Elia, E. Aqueous Extracts of the Castor Beans as a Corrosion Inhibitor of Mild Steel in HCl Media. *J. Braz. Chem. Soc.* **2020**, *31*, 1225–1238. [[CrossRef](#)]
- Umoren, S.A.; Solomon, M.M.; Obot, I.B.; Suleiman, R.K. Critical review on the recent studies on plant biomaterials as corrosion inhibitors for industrial metals. *J. Ind. Eng. Chem.* **2019**, *25*, 91–115. [[CrossRef](#)]
- Matos, L.A.C.; Tabora, M.C.; Alves, G.J.T.; Cunha, M.T.; Banczek, E.P.; Oliveira, M.F.; D'Elia, E.; Rodrigues, P.R.P. Application of an acid extract of Barley agro-industrial waste as a corrosion inhibitor for stainless steel AISI 304 in H<sub>2</sub>SO<sub>4</sub>. *Int. J. Electrochem. Sci.* **2018**, *13*, 1577–1593. [[CrossRef](#)]
- Khan, G.; Basirun, W.J.; Kazi, S.N.; Ahmed, P.; Magaji, L.; Ahmed, S.M.; Khan, G.M.; Rehman, M.A.; Badrya, A.B.B.M. Electrochemical investigation on the corrosion inhibition of mild steel by Quinazoline Schiff base compounds in hydrochloric acid solution. *J. Colloid Interface Sci.* **2017**, *502*, 134–145. [[CrossRef](#)] [[PubMed](#)]
- Hassannejad, H.; Nouri, A. Sunflower seed hull extract as a novel green corrosion inhibitor for mild steel in HCl solution. *J. Mol. Liq.* **2018**, *254*, 377–382. [[CrossRef](#)]
- Nita, C.; Zhangd, B.; Dentzera, J.; Ghimbeu, C.M. Hard carbon derived from coconut shells, walnut shells, and corn silk biomass waste exhibiting high capacity for Na-ion batteries. *J. Energy Chem.* **2021**, *58*, 207–218. [[CrossRef](#)]
- Zhao, W.; Wen, J.; Zhao, Y.; Wang, Z.; Shi, Y.; Zhao, Y. Hierarchically Porous Carbon Derived from Biomass Reed Flowers as Highly Stable Li-Ion Battery Anode. *Nanomaterials* **2020**, *10*, 346. [[CrossRef](#)]
- Wang, Z.; Zhang, X.; Liu, X.; Zhang, Y.; Zhao, W.; Li, Y.; Qin, C.; Bakenov, Z. High specific surface area bimodal porous carbon derived from biomass reed flowers for high performance lithium-sulfur batteries. *J. Colloid Interface Sci.* **2020**, *569*, 22–33. [[CrossRef](#)] [[PubMed](#)]
- Marzorati, S.; Verotta, L.; Trasatti, S.P. Green Corrosion Inhibitors from Natural Sources and Biomass Wastes. *Molecules* **2018**, *24*, 48. [[CrossRef](#)]
- Andrade, J.C.; Silva, A.R.P.; Santos, A.T.L.; Freitas, M.A.; Carneiro, J.N.P.; Gonçalo, M.I.P.; de Souza, A.; Freitas, T.S.; Ribeiro, P.R.V.; Brito, E.S.; et al. UPLC-MS-ESI-QTOF characterization and evaluation of the antibacterial and modulatory antibiotic activity of *Ziziphus joazeiro* Mart. aqueous extracts. *S. Afr. J. Bot.* **2019**, *23*, 105–112. [[CrossRef](#)]
- Andrade, J.C.; Silva, A.R.P.; Santos, A.T.L.; Freitas, M.A.; Matos, Y.M.L.S.; Morais, M.F.B.; Bezerra, C.F.; Gonçalo, M.I.P.; Gomez, M.C.V.; Rolóm, M.; et al. Chemical composition, antiparasitic and cytotoxic activities of aqueous extracts of *Ziziphus joazeiro* Mart. *Asian Pac. J. Trop. Biomed.* **2019**, *5*, 222–226.
- Andrade, J.C.; Silva, A.R.P.; Santos, A.T.L.; Freitas, M.A.; Ramos, B.A.; Freitas, T.S.; dos Santos, F.A.G.; Leite-Andrade, M.C.; Nunes, M.; Tintino, S.R.; et al. Control of bacterial and fungal biofilms by natural products of *Ziziphus joazeiro* Mart. (Rhamnaceae). *Comp. Immunol. Microbiol. Infect. Dis.* **2019**, *65*, 226–233. [[CrossRef](#)] [[PubMed](#)]
- Ikeuba, A.I.; Okafor, P.C. Green corrosion protection for mild steel in acidic media: Saponins and crude extracts of *Gongronema latifolium*. *Pigment Resin Technol.* **2019**, *48*, 57–64. [[CrossRef](#)]
- Gopal, J.; Dwivedi, P.; Sundaram, S.; Prakash, R. Inhibitive Effect of Chlorophytum Borivilianum Root Extract on Mild Steel Corrosion in HCl and H<sub>2</sub>SO<sub>4</sub> Solutions. *Ind. Eng. Chem. Res.* **2013**, *52*, 10673–10681.
- Ugi, B.U.; Obeten, M.E.; Magu, T.O. Phytochemical constituents of Taraxacum officinale leaves as eco-friendly and nontoxic organic inhibitors for stainless steel corrosion in 0.2 M HCl acid medium. *Int. J. Chem. Sci.* **2018**, *2*, 35–43.
- Ugi, B.U.; Magu, T.O. Inhibition, Adsorption and Thermodynamic Investigation of Iron Corrosion by Green Inhibitors in Acidic Medium. *Int. J. Sci. Technol.* **2017**, *5*, 56–64.
- Pluskal, T.; Castillo, S.; Villar-Briones, A.; Orešič, M. MZmine 2: Modular framework for processing, visualizing, and analyzing mass spectrometry-based molecular profile data. *BMC Bioinform.* **2010**, *11*, 395. [[CrossRef](#)] [[PubMed](#)]
- Nothias, L.; Petras, D.; Schmid, R.; Dührkop, K.; Rainer, J.; Sarvepalli, A.; Protzyuk, I.; Ernst, M.; Tsugawa, H.; Fleischauer, M.; et al. Feature-based molecular networking in the GNPS analysis environment. *Nat. Methods* **2020**, *17*, 905–908. [[CrossRef](#)]

19. Shannon, P.; Markiel, A.; Ozier, O.; Baliga, N.S.; Wang, J.T.; Ramage, D.; Amin, N.; Schwikowski, B.; Ideker, T. Cytoscape: A software environment for integrated models of biomolecular interaction networks. *Genome Res.* **2003**, *13*, 2498–2504. [[CrossRef](#)]
20. Herzog, R.; Schwudke, D.; Shevchenko, A. LipidXplorer: Software for Quantitative Shotgun Lipidomics Compatible with Multiple Mass Spectrometry Platforms. *Curr. Protoc. Bioinform.* **2013**, *43*, 14.12.1–14.12.30. [[CrossRef](#)]
21. Borges, R.M.; Taujale, R.; de Souza, J.S.; Bezerra, T.A.; Silva, E.L.; Herzog, R.; Ponce, F.V.; Wolfender, J.-L.; Edison, A.S. Dereplication of plant phenolics using a mass-spectrometry database independent method. *Phytochem. Anal.* **2018**, *29*, 601–612. [[CrossRef](#)] [[PubMed](#)]
22. Soares, V.; Taujale, R.; Garrett, R.; da Silva, A.J.R.; Borges, R.M. Extending compound identification for molecular network using the LipidXplorer database independent method: A proof of concept using glycoalkaloids from *Solanum pseudoquina* A. St.-Hil. *Phytochem. Anal.* **2019**, *30*, 132–138. [[CrossRef](#)] [[PubMed](#)]
23. Tsugawa, H.; Cajka, T.; Kind, T.; Ma, Y.; Higgins, B.; Ikeda, K.; Kanazawa, M.; Vander Gheynst, J.; Fiehn, O.; Arita, M. MS-DIAL: Data-independent MS/MS deconvolution for comprehensive metabolome analysis. *Nat. Methods* **2015**, *12*, 523–526. [[CrossRef](#)] [[PubMed](#)]
24. Shiau, I.L.; Shih, T.L.; Wang, Y.N.; Chen, H.T.; Lan, H.F.; Lin, H.C.; Yang, B.-Y.; Ko, C.-H.; Murase, Y. Quantification for saponin from Soapberry (*Sapindus mukorossi* Gaertn) in cleaning products by a Chromatographic and two colorimetric assays. *J. Fac. Agric. Kyushu Univ.* **2009**, *54*, 215–221. [[CrossRef](#)]
25. Frisch, M.J.; Trucks, G.; Schlegel, H.B.; Scuseria, G.E.; Robb, M.A.; Cheeseman, J.R.; Scalmani, G.; Barone, V.; Petersson, G.A.; Nakatsuji, H.; et al. *Gaussian 09, Revision A.02*; Gaussian: Wallingford, CT, USA, 2016.
26. Becke, A.D. Density-functional thermochemistry. III. The role of exact exchange. *J. Chem. Phys.* **1993**, *98*, 5648–5652. [[CrossRef](#)]
27. Lee, C.; Yang, W.; Parr, R.G. Development of the Colle-Salvetti correlation-energy formula into a functional of the electron density. *Phys. Rev. B* **1988**, *37*, 785–789. [[CrossRef](#)]
28. Hay, P.J.; Wadt, W.R. Ab initio effective core potentials for molecular calculations. Potentials for K to Au including the outermost core orbitals. *J. Chem. Phys.* **1985**, *82*, 299–310. [[CrossRef](#)]
29. Márquez-Sánchez, J.; Zorrilla, D.; Sánchez-Coronilla, A.; De Los Santos, D.M.; Navas, J.; Fernández-Lorenzo, C.; Alcántara, R.; Martín-Calleja, J. Introducing “UCA-FUKUI” software: Reactivity-index calculations. *J. Mol. Model.* **2014**, *20*, 2492. [[CrossRef](#)]
30. Chauhan, D.S.; Quraishi, M.A.; Sorour, A.A.; Saha, S.K.; Banerjee, P. Triazole-modified chitosan: A biomacromolecule as a new environmentally benign corrosion inhibitor for carbon steel in a hydrochloric acid solution. *RSC Adv.* **2019**, *9*, 14990–15003. [[CrossRef](#)]
31. Nuengchamnon, N.; Sookying, S.; Ingkaninan, K. LC-ESI-QTOF-MS based screening and identification of isomeric jujubogenin and pseudojujubogenin aglycones in *Bacopa monnieri* extract. *J. Pharm. Biomed. Anal.* **2016**, *129*, 121–134. [[CrossRef](#)]
32. Ma, J.-J.; Kang, L.-P.; Zhou, W.-B.; Yu, H.-S.; Liu, P.; Ma, B.-P. Identification and characterization of saponins in extract of *Ziziphispinosae* Semen (ZSS) by ultra-performance liquid chromatography-electrospray ionization-quadrupole time-of-flight tandem mass spectrometry (UPLC-ESI-QTOF-MSE). *J. Med. Plants Res.* **2011**, *5*, 6152–6159.
33. Andrade, J.C.; Santos, A.T.L.; Silva, A.R.P.; Freitas, M.A.; Afza, M.I.; Gonçalo, M.I.P.; Fonseca, V.J.A.; Costa, M.S.; Carneiro, J.N.P.; Sousa, E.O.; et al. Phytochemical characterization of the *Ziziphus joazeiro* Mart. metabolites by UPLCQTOF and antifungal activity evaluation. *Cell. Mol. Biol.* **2020**, *66*, 127–132. [[CrossRef](#)]
34. Grosvenor, A.P.; Kobe, B.A.; Biesinger, M.C.; McIntyre, N.S. Investigation of multiplet splitting of Fe 2p XPS spectra and bonding in iron compounds. *Surf. Interface Anal.* **2004**, *36*, 1564–1574. [[CrossRef](#)]
35. Rahiman, F.S.A.; Sethumanickam, S. Corrosion inhibition, adsorption and thermodynamic properties of poly(vinyl alcoholcysteine) in molar HCl. *Arabian. J. Chem.* **2017**, *10*, S3358–S3366.
36. Garai, S. Advances in Triterpenoid Saponins Research 2007–2012. *Herb. Med.* **2016**, *2*, 2472–0151. [[CrossRef](#)]
37. Fernandes, C.M.; Fagundes, T.S.F.; Santos, N.E.; Rocha, T.S.M.; Garrett, R.; Borges, R.M.; Muricy, G.; Valverde, A.L.; Ponzio, E.A. *Irciniastrobilina* crude extract as corrosion inhibitor for mild steel in acid medium. *Electrochim. Acta* **2019**, *312*, 137–148. [[CrossRef](#)]
38. Hamdy, A.; El-Gendy, N.S. Thermodynamic, adsorption and electrochemical studies for corrosion inhibition of carbon steel by henna extract in acid medium. *Egypt. J. Pet.* **2013**, *22*, 17–25. [[CrossRef](#)]
39. Rodrigues, L.S.; do Valle, A.F.; D’Elia, E. Biomass of microalgae *Spirulina Maxima* as a corrosion inhibitor for 1020 carbon steel in acidic solution. *Int. J. Electrochem. Sci.* **2018**, *13*, 6169–6189. [[CrossRef](#)]
40. Cordeiro, R.F.B.; Belati, A.J.S.; Perrone, D.; D’Elia, E. Coffee husk as corrosion inhibitor for mild steel in HCl media. *Int. J. Electrochem. Sci.* **2018**, *13*, 12188–12207. [[CrossRef](#)]
41. Sivakumara, V.; Velumania, K.; Rameshkumara, S. ColocidDye-A Potential Corrosion Inhibitor for the Corrosion of Mild Steel in Acid Media. *Mater. Res.* **2018**, *21*, e20170167.
42. Guimarães, T.A.S.; Cunha, J.N.; Oliveira, G.A.; Silva, T.U.; Oliveira, S.M.; Araújo, J.R.; Machado, S.P.; D’Elia, E. Nitrogenated derivatives of furfural as green corrosion inhibitors for mild steel in HCl solution. *J. Mater. Res. Technol.* **2020**, *9*, 7104–7122. [[CrossRef](#)]
43. Kuznetsov, Y.I.; Andreev, N.N.; Vesely, S.S. Why we reject papers with calculations of inhibitor adsorption based on data on protective effects. *Int. J. Corros. Scale Inhib.* **2015**, *4*, 108. [[CrossRef](#)]
44. Danaee, I.; RameshKumar, S.; RashvandAvei, M.; Vijayan, M. Electrochemical and Quantum Chemical Studies on Corrosion Inhibition Performance of 2,2’-(2-Hydroxyethylimino)bis[N-(alpha-alpha-dimethylphenethyl)-N-methylacetamide] on Mild Steel Corrosion in 1M HCl Solution. *Mater. Res.* **2020**, *23*, 1–16. [[CrossRef](#)]

45. Ituen, E.; Akaranta, O.; James, A. Evaluation of Performance of Corrosion Inhibitors Using Adsorption Isotherm Models: An Overview. *Chem. Sci. Int. J.* **2017**, *18*, 1–34. [[CrossRef](#)]
46. Uwah, I.E.; Okafor, P.C.; Ebiekpe, U.E. Inhibitive action of ethanol extracts from *Nauclealatifolia* on the corrosion of mild steel in H<sub>2</sub>SO<sub>4</sub> solutions and their adsorption characteristics. *Arab. J. Chem.* **2013**, *6*, 285–293. [[CrossRef](#)]
47. El-Awady, A.A.; Abd-El-Nabey, B.A.; Aziz, S.G. Kinetic thermodynamic and adsorption isotherms analyses for the inhibition of the acid corrosion of steel by cyclic and open-chain amines. *J. Electrochem. Soc.* **1992**, *139*, 2149. [[CrossRef](#)]
48. Eddy, N.O.; Ebenso, E.E.; Ibok, U.J.; Akpan, E.E. Experimental and Computational Chemistry studies on the inhibition of the Corrosion of Mild Steel in H<sub>2</sub>SO<sub>4</sub> by (2s,5s,6r)-6-(2-(aminomethyl)-5-(3-(2-chlorophenyl)isoxazol-5-yl)benzamido)-3,3-dimethyl-7-oxo-4-thia-1-azabicyclo[3.2.0]heptane-2-carboxylic acid. *Int. J. Electrochem. Sci.* **2011**, *6*, 4296–4315.
49. Ansari, K.R.; Quraishi, M.A.; Singh, A.; Ramkumar, S.; Obote, I.B. Corrosion inhibition of N80 steel in 15% HCl by pyrazolone derivatives: Electrochemical, surface and quantum chemical studies. *RSC Adv.* **2016**, *6*, 24130–24141. [[CrossRef](#)]